Supplementary Information for

Quantifying quantum coherence of multiple-charge states in tunable Josephson junctions

Jiangbo He[1,#], Dong Pan[2,#], Mingli Liu[1,3], Zhaozheng Lyu[1,4], Zhongmou Jia[1,3], Guang Yang[1], Shang Zhu[1,3], Guangtong Liu[1,4,5], Jie Shen[1,5], Sergey N. Shevchenko[6], Franco Nori[7,8,9,*], Jianhua Zhao[2,*], Li Lu[1,3,4,5,*], Fanming Qu[1,3,4,5,*]

[1] *Beijing National Laboratory for Condensed Matter Physics, Institute of Physics, Chinese Academy of Sciences, Beijing 100190, China*

[2] *State Key Laboratory of Superlattices and Microstructures, Institute of Semiconductors, Chinese Academy of Sciences, P.O. Box 912, Beijing 100083, China*

[3] *School of Physical Sciences, University of Chinese Academy of Sciences, Beijing 100049, China*

[4] *Hefei National Laboratory, Hefei 230088, China*

[5] *Songshan Lake Materials Laboratory, Dongguan 523808, China*

[6] *B. Verkin Institute for Low Temperature Physics and Engineering, Kharkiv 61103, Ukraine*

[7] *Theoretical Quantum Physics Laboratory, Cluster for Pioneering Research, RIKEN, Wakoshi, Saitama, 351-0198, Japan*

[8] *Quantum Computing Center, RIKEN, Wakoshi, Saitama, 351-0198, Japan*

[9] *Physics Department, The University of Michigan, Ann Arbor, MI 48109-1040, USA*

[#] These authors contributed equally to this work.

[*] Email: fnori@riken.jp; jhzhao@semi.ac.cn; lilu@iphy.ac.cn; fanmingqu@iphy.ac.cn

Contents

Supplementary Note 1. Growth of the epitaxial nanowires.

In this work, all the nanowires were grown on p-type Si (111) substrates. The <111> and non-<111>-oriented $InAs_{0.92}Sb_{0.08}$-Al nanowires coexisted on the substrate surface because the thin natural oxide layer on the Si substrates cannot be removed completely before the nanowire growth. According to detailed transmission electron microscope (TEM) observations, we find that continuous half Al shells can be successfully grown on the facets of $InAs_{0.92}Sb_{0.08}$ nanowires with non-<111> growth directions, while the Al shells are discontinuous and look like 'pearls on a string' on the side walls of the <111> oriented nanowires. Particularly, narrow Al gaps can form naturally in these non-<111> $InAs_{0.92}Sb_{0.08}$-Al nanowires due to shadowing between the dense nanowires. Supplementary Figure 1 shows a high-angle annular dark-field scanning transmission electron microscope (HAADF-STEM), energy dispersive spectrum (EDS) and high-resolution TEM data of a typical shadow $InAs_{0.92}Sb_{0.08}$-Al nanowire. As shown in Supplementary Figure 1a, a half Al shell with a narrow Al gap can be clearly observed on the facet of the $InAs_{0.92}Sb_{0.08}$ nanowire. The false-color EDS elemental maps of In (Supplementary Figure 1b), As (Supplementary Figure 1c), Sb (Supplementary Figure 1d) and Al (Supplementary Figure 1e) of the $InAs_{0.92}Sb_{0.08}$-Al nanowire further confirm that a narrow Al gap indeed formed in the continuous Al shell. Supplementary Figures 1f and 1g are high-resolution TEM images of the nanowire taken from the $InAs_{0.92}Sb_{0.08}$ region and $InAs_{0.92}Sb_{0.08}$-Al interface area, respectively. The $InAs_{0.92}Sb_{0.08}$ nanowire has a pure zinc-blende crystal structure due to its non-<111> growth direction, although the Sb content is low, which is consistent with our previous work[1]. As shown in Supplementary Figure 1g, an abrupt interface between the Al shell and the $InAs_{0.92}Sb_{0.08}$ nanowire can be observed.

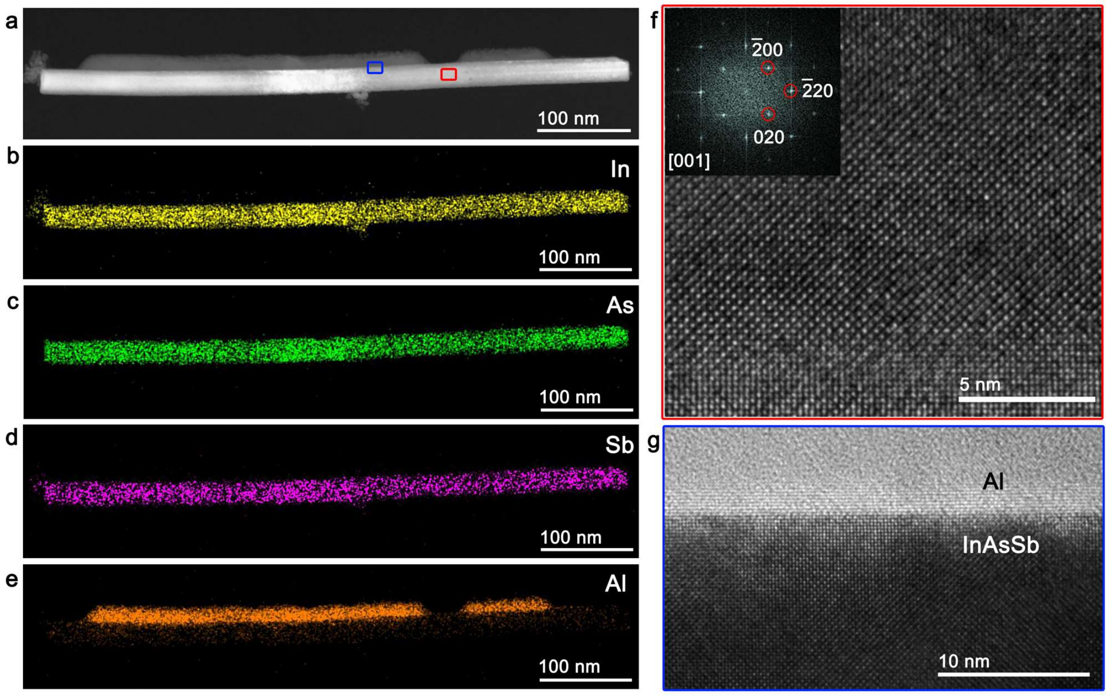

Supplementary Figure 1. Chemical composition and crystal structure of the $InAs_{0.92}Sb_{0.08}$-Al nanowires. a, HAADF-STEM image of an $InAs_{0.92}Sb_{0.08}$-Al nanowire. **b-e,** False-color EDS elemental maps of In (yellow), As (green), Sb (purple), and Al (orange) of the $InAs_{0.92}Sb_{0.08}$-Al nanowire, respectively. **f,** High-resolution TEM image of the $InAs_{0.92}Sb_{0.08}$ nanowire. The inset of **f** is its corresponding fast Fourier transform. **g,** High-resolution TEM image of the $InAs_{0.92}Sb_{0.08}$ nanowire taken from the $InAs_{0.92}Sb_{0.08}$-Al interface area. The blue and red rectangles in **a** highlight the regions where high-resolution TEM images were recorded.

Supplementary Note 2. Measurement setup.

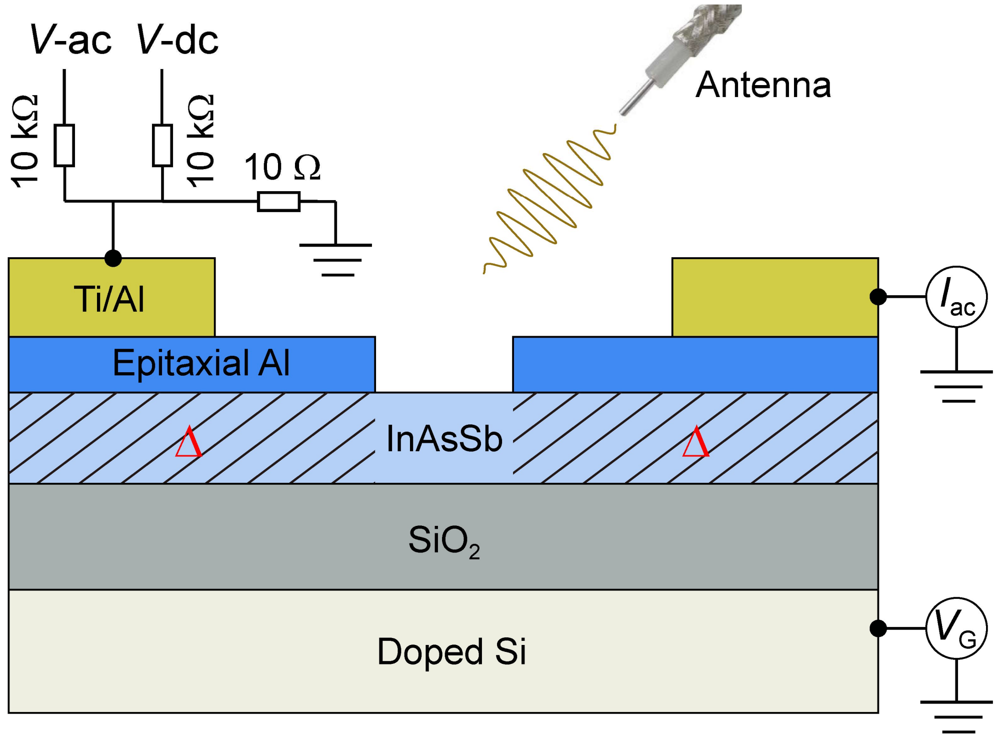

Supplementary Figure 2. The measurement setup.

Supplementary Figure 2 shows the transport measurement setup. A small ac voltage V-ac and a dc voltage V-dc were applied through a voltage divider, after which the actual V_{ac} and V_b were subjected onto the device. The ac current I_{ac} was measured. A serial resistance from the dc wires and the low-pass filters was subtracted during the data analysis. A gate voltage V_G was applied through a 300 nm-thick SiO_2 to control the coupling strength of the Josephson junction (JJ). The shaded InAsSb nanowire segments were brought into proximity with the epitaxial Al to possess a hard superconducting gap of size Δ. A microwave antenna with an open end of a coaxial cable was implemented to radiate the junction with microwaves. For the critical current measurement and the Shapiro step measurement, the dc current was converted.

Supplementary Note 3. Theoretical treatment of the LZSM interference.

In this section, we interpret the theoretical treatment of the LZSM interference in the small JJ studied in our work. For ease of reading, we illustrate the LZSM interference again in Supplementary Figures 3a-3c. As explained in the main text, we map the effective two states as the charges being on the left and the right side of the junction based on the Bardeen-Cooper-Schrieffer singularities of the density of states (see Supplementary Figure 3a for the case of Cooper pairs). The coupling strength between the two states, |L> and |R>, is defined as $\alpha/2$, resulting in an anti-crossing of α. The red and blue energy levels in Supplementary Figure 3b are thus the two effective levels for LZSM interference. We consider a harmonic microwave driving with an amplitude of V_{RF} and a frequency of f. The detuning can be controlled by applying a bias voltage relative to the anti-crossing point, V_0. As displayed in Supplementary Figures 3b and 3c, a LZSM transition takes place at time t_1 and (after accumulating a phase difference of θ) a subsequent LZSM transition and LZSM interference occur at time t_2, when the system is driven back to the anti-crossing point.

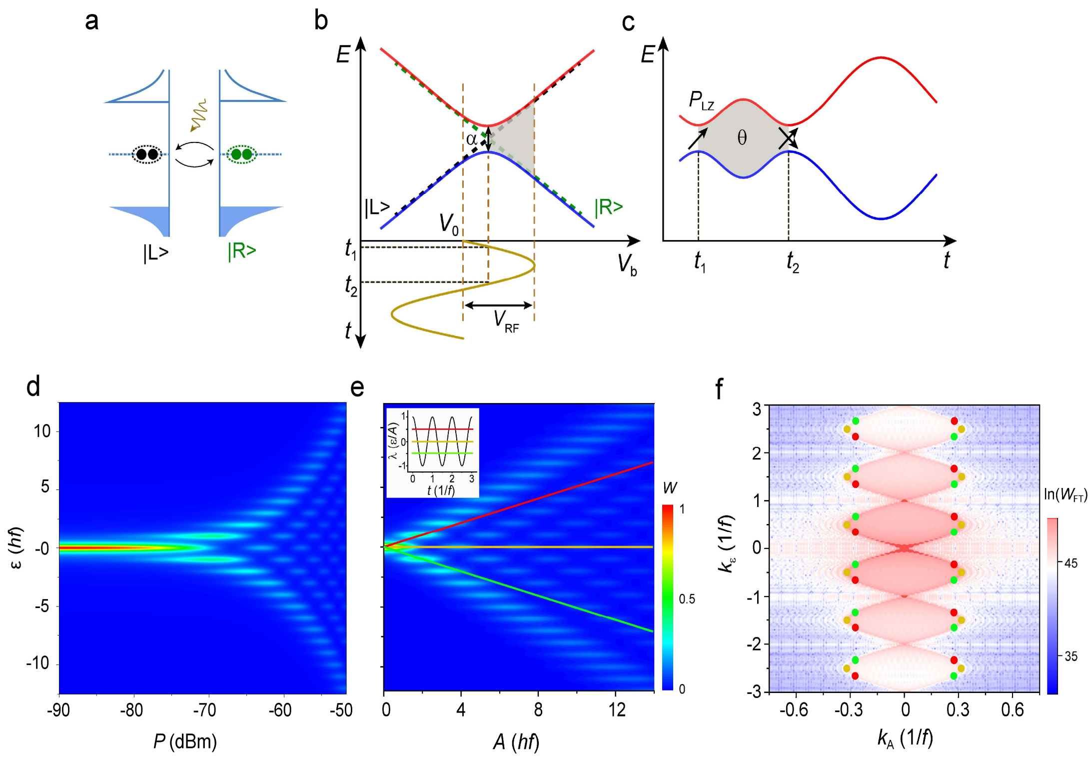

Supplementary Figure 3. LZSM interference and its Fourier transform. a, Illustration of the two effective states in a small JJ. **b, c**, Schematics of the two-level system and the microwave driven LZSM interference. **d**, **e,** Calculated interference fringes. A harmonic driving signal (inset in **e**) with a frequency f = 10 GHz, and a decoherence rate $\Gamma_2 = 1/(4\omega)$ ($\omega = 2\pi f$) were used. **f**, The two-dimensional Fourier transform (2DFT) of **e**. The colored dots stand for the corresponding contributions from the lines in **e**.

The extraction of the coherence time in Fourier space for a driven qubit has been theoretically studied by Rudner et al[2]. Here we follow a similar procedure and theoretically analyze the LZSM interference for various charges in our small JJs. When a harmonic drive $V_{\mathrm{RF}}\cos(\omega t)$ ($\omega = 2\pi f$) is applied, the Hamiltonian of the system can be expressed as:

$$H = -\frac{\hbar}{2}\begin{pmatrix} \beta(t) & \alpha \\ \alpha & -\beta(t) \end{pmatrix}, \quad \beta(t) = \varepsilon - A\cos(\omega t), \tag{1}$$

where $\varepsilon = meV_0$, $A = meV_{\mathrm{RF}}$, m is the number of charges, and e is the elementary charge. When $V_{\mathrm{RF}} > V_0$, the system will be driven to pass through the anti-crossing twice at t_1 and t_2 in one period, respectively. The times $t_{1,2}$ satisfy

$$A\cos(\omega t_1) = A\cos(\omega t_2) = \varepsilon, \qquad \left(-1 < \frac{\varepsilon}{A} < 1\right). \tag{2}$$

The phase difference (gray shaded area in Supplementary Figure 3c) accumulated between the two LZ transitions can be expressed as:

$$\theta(A,\varepsilon) = \int_{t_1}^{t_2} \beta(t)\mathrm{d}t = \varepsilon(t_2 - t_1) - A\int_{t_1}^{t_2} \cos(\omega t)\mathrm{d}t. \tag{3}$$

Let us define a wave vector in the time domain

$$(k_A, k_\varepsilon) = \pm\big(\nabla_A\theta(A,\varepsilon), \nabla_\varepsilon\theta(A,\varepsilon)\big), \tag{4}$$

where $\pm$ accounts for the contributions of $\mathrm{e}^{\pm\mathrm{i}\theta(A,\varepsilon)}$. Considering that the net contributions of $\nabla_A t_{1,2}$ and $\nabla_\varepsilon t_{1,2}$ vanish due to Eq. (2),

$$(k_A, k_\varepsilon) = \pm\left(-\int_{t_1}^{t_2} \cos(\omega t)\,\mathrm{d}t\,, t_2 - t_1\right). \tag{5}$$

Obviously, k_A and k_ε correspond to the phase gain and the time separation, respectively. The solution of Eq. (2), $t_2 = -t_1 = \frac{1}{\omega}\arccos(\varepsilon/A)$, gives $\int_{t_1}^{t_2} \cos(\omega t)\mathrm{d}t = (2/\omega)\sqrt{1 - \varepsilon^2/A^2}$. Therefore, Eq. (5) defines a curve that is dependent only on the parameter $\lambda = \varepsilon/A$. Substituting these results into Eq. (5), we obtain that the parametric curve is a sine function

$$\omega\frac{k_A}{2} = \pm\sin\left(\frac{\omega k_\varepsilon}{2}\right). \tag{6}$$

As explained later, this function corresponds to the lemon-shaped ovals with a singular boundary in the 2DFT (k_A, k_ε) space of the interference fringes (see also Supplementary Figure 3f).

To account for decoherence, a classical noise can be added to the microwave drive, $\tilde{\beta}(t) = \beta(t) + \delta\varepsilon(t)$. The rate of transitions between |L> and |R> can be easily deduced in a rotating frame, where we have

$$H = -\frac{\hbar}{2}\begin{pmatrix} 0 & \alpha(t) \\ \alpha^*(t) & 0 \end{pmatrix}, \qquad \alpha(t) = \alpha \mathrm{e}^{-\mathrm{i}\tilde{\theta}(t)}, \tag{7}$$

with $\tilde{\theta}(t) = \int_0^t \tilde{\beta}(t')\mathrm{d}t'$. The rate of transitions between |L> and |R> is

$$W = \lim_{\delta t \Gamma_2 \gg 1} \frac{\alpha^2}{4\delta t} \iint_t^{t+\delta t} \langle \mathrm{e}^{-\mathrm{i}\tilde{\theta}(t_1)} \mathrm{e}^{\mathrm{i}\tilde{\theta}(t_2)} \rangle_{\delta\varepsilon} \, \mathrm{d}t_1 \mathrm{d}t_2, \tag{8}$$

where $\Gamma_2 = \frac{1}{T_2}$ is the decoherence rate. A white noise model can be applied to average over $\delta\varepsilon(t)$: $\langle \mathrm{e}^{\mathrm{i}\delta \ (t_2) - \mathrm{i}\delta\theta(t_1)} \rangle_{\delta\varepsilon} = \mathrm{e}^{-\Gamma_2 |t_1 - t_2|}$, where $\delta\theta(t) = \int_0^t \delta\varepsilon(t')\mathrm{d}t'$.

The Fourier series expansion, $\mathrm{e}^{\mathrm{i}\theta(t)} = \mathrm{e}^{\mathrm{i}\varepsilon t} \sum_n J_n\left(\frac{A}{\omega}\right) \mathrm{e}^{-\mathrm{i}n\omega t}$, where J_n is a Bessel function of the first kind, can be used to obtain

$$W(\varepsilon, A) = \frac{\alpha^2}{2} \sum_{n=-\infty}^{+\infty} \frac{\Gamma_2 \ J_n^2\left(\frac{A}{\hbar\omega}\right)}{(\varepsilon - n\hbar\omega)^2 + \hbar^2 \Gamma_2^2}. \tag{9}$$

It is this equation, Eq. (9), that relates to the conductance of the JJ, a measurable parameter in the experiment. It describes the interference fringes as a function of the microwave drive $A = meV_{\mathrm{RF}}$ and the detuning (voltage bias) $\varepsilon = meV_0$ relative to the anti-crossing point. Supplementary Figure 3e presents one example calculated directly from Eq. (9), using a frequency $f = 10$ GHz and a decoherence rate $\Gamma_2 = 1/(4\omega)$. Note that the data has been scaled to a maximum of 1, and the x-axis is the microwave amplitude V_{RF} ($A = meV_{\mathrm{RF}}$), while in our measured data it is the power P. In addition, along the y-axis, the spacing δV_{b} of the satellite peaks satisfies $hf = me\delta V_{\mathrm{b}}$ [or $\delta V_{\mathrm{b}} = (hf/e)(1/m)$], which enables a direct extraction of the number of charges m for the various tunneling processes in our experiment.

The Fourier transform, $W_{\mathrm{FT}}(k_A, k_\varepsilon) = \int_{-\infty}^{+\infty} \mathrm{e}^{-\mathrm{i}k_A A - \mathrm{i}k_\varepsilon \varepsilon} W(A, \varepsilon)\, \mathrm{d}A\mathrm{d}\varepsilon$, maps $W(\varepsilon, A)$ from the energy space to the Fourier space in the time domain[2],

$$W_{\mathrm{FT}}(k_A, k_\varepsilon) = \frac{\alpha^2 \omega\, \mathrm{e}^{-\Gamma_2 |k_\varepsilon|}}{2\sqrt{\frac{4}{\omega^2} \sin^2\left(\frac{1}{2}\omega k_\varepsilon\right) - k_A^2}}. \tag{10}$$

We can see that $W_{\mathrm{FT}}(k_A, k_\varepsilon)$ is concentrated inside the region bounded by the sinusoids $\frac{\omega}{2} k_A = \pm \sin\left(\frac{1}{2}\omega k_\varepsilon\right)$, which is the Eq. (6) shown above. Therefore, lemon-shaped ovals following such singular boundary are expected in Fourier space. Crucially, an exponential decay on k_ε as $\mathrm{e}^{-\Gamma_2 |k_\varepsilon|}$ can help to directly extract the coherence time T_2, which demonstrates that this is a powerful technique.

Supplementary Figure 3f shows the 2DFT results of Supplementary Figure 3e. Note that the integral to obtain W_{FT} is from $-\infty$ to $+\infty$; therefore, the fringes shown in Supplementary Figure 3e need to be symmetrized to the four quadrants before performing the 2DFT. Lemon-shaped ovals are consistent with Eq. (10) and also with our experimental results. In addition, for a given λ, there is a ray $\varepsilon = \lambda A$ in energy space (A, ε) and a set of periodic points in the temporal space. As shown in Supplementary Figures 3e and 3f, the colored rays of the interference fringes contribute to the colored dots in the Fourier space correspondingly. For example, the red ray stands for $\varepsilon = \frac{1}{2} A$, and accordingly,

$$(k_A, k_\varepsilon) = \pm\left(-\left(\frac{2}{\omega}\right)\sqrt{1 - \frac{\varepsilon^2}{A^2}},\ \frac{2}{\omega}\arccos\left(\frac{\varepsilon}{A}\right)\right) = \pm\left(-\frac{\sqrt{3}}{2\pi f},\ \frac{1}{3f}\right).$$

Next, we show that these results can be directly compared with a recent theoretical derivation of the conductance considering sub-gap Yu-Shiba-Rusinov (YSR or Andreev) states, and we can reach a consistent conclusion.

In Ref. 3, the authors adopted the photon-assisted picture to calculate the tunneling conductance to sub-gap states in a superconductor and obtained the following results.

(1) They obtained the conductance between a normal probe and the YSR states at zero temperature,

$$\frac{dI}{dV} = \frac{2e^2}{h} \sum_{\pm} \frac{\gamma_{\mathrm{e}}\gamma_{\mathrm{h}}}{(eV \pm \epsilon_0)^2 + (\gamma_{\mathrm{e}} + \gamma_{\mathrm{h}})^2/4}, \tag{11}$$

where γ_{e} and γ_{h} are the tunneling rates of electrons and holes, respectively, and ϵ_0 is the energy of the sub-gap states. We can see that (without microwave radiation) the conductance peak shows a Lorentzian shape, where the tunneling rates (coupling strength) function as the broadening term. Note that the appearance of two tunneling rates, γ_{e} and γ_{h}, is a specific requirement of YSR states, and $\alpha/2$ is the coupling strength in our model.

(2) The conductance $\mathrm{d}I/\mathrm{d}V$ was further obtained under microwave radiation,

$$\frac{dI}{dV} = \frac{2e^2}{h} \sum_{n} \sum_{\pm} \frac{J_n^2(eV_{\mathrm{HF}}/\hbar\Omega)\gamma_{\mathrm{e}}\gamma_{\mathrm{h}}}{(eV + n\hbar\Omega \pm \epsilon_0)^2 + (\gamma_{\mathrm{e}} + \gamma_{\mathrm{h}})^2/4}. \tag{12}$$

We found that Eq. (12) in this theoretical work is fundamentally the same as the result of Eq. (9) in our work. For example, if we consider the transport of single charges at $V_{\mathrm{b}} = 2\Delta/e$, the number of electrons transferred from the left side to the right side of the Josephson junction per unit time is W, i.e., the conductance is proportional to W.

The difference between Eq. (9) and Eq. (12) obtained in Ref. 3 is that in the denominator the tunneling rate (γ_e and γ_h; coupling strength) is the broadening term in the latter; but in our case it is the decoherence rate Γ_2. In the photon-assisted picture, the main broadening factor is the tunnel coupling. However, in the LZSM model, it includes various sources, such as tunnel coupling, thermal broadening, noise, etc. Therefore, we can call it a full-counting model which treats all the broadening/decoherence factors in the Lorentzian shape. In this case, what we care about is the shape (broadening) of the conductance peak which tells us the coherence/decoherence information, but not the absolute peak height (the background conductance may be involved in a realistic measurement). The Bessel function dependence of the evolution of the conductance peaks under microwave driving is clearly present in both pictures.

Supplementary Note 4. Choice of the microwave frequencies.

In order to choose proper frequencies of the microwave, we measured the dI/dV dependence on both the microwave frequency f and power P at a back-gate voltage $V_G = -30$ V and a bias voltage near the gap edge, as shown in Supplementary Figure 4. There is a clear frequency-dependent effective attenuation of the microwave, presumably due to the coaxial lines and the details of the coupling between the microwave and the device. Nevertheless, in order to get rid of the heat load on the dilution refrigerator, we selected frequencies corresponding to a local minimum attenuation, as marked by the green arrows for 7.665 GHz and 11.755 GHz, respectively.

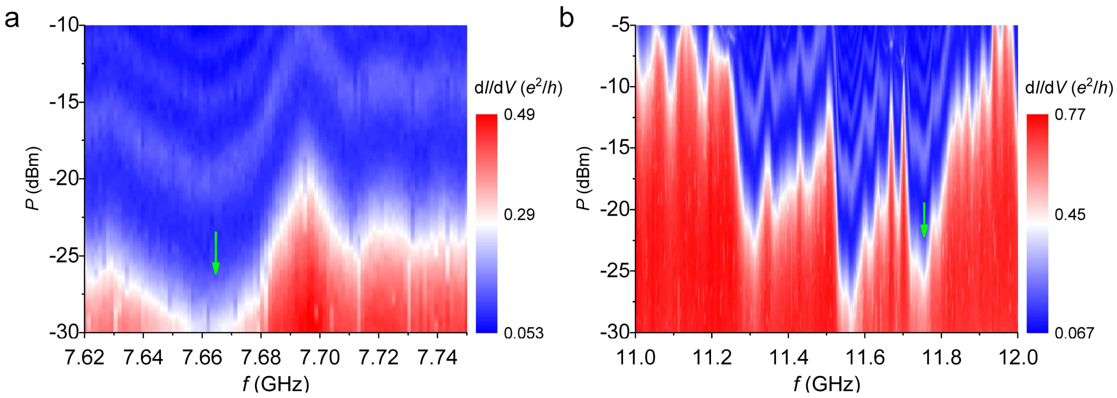

Supplementary Figure 4. Choice of the microwave frequencies. The dI/dV was measured as a function of the microwave frequency f and power P using a back-gate voltage $V_G = -30$ V and a bias voltage near the gap edge.

Supplementary Note 5. Data analysis

In this section, we explain the data analysis process of the interference fringes. As an example, here we study the data shown in Fig. 2c in the main text for $V_G = -31$ V and $f = 11.755$ GHz.

Step 1: determine the attenuation of the microwave.

As shown in Supplementary Note 4, there is a frequency-dependent attenuation of the microwave. Therefore, we need to determine the actual microwave power experienced by the junction for each frequency used in the experiment. For instance, by applying Eq. (9) we calculated the interference fringes for single charges at $V_G = -31$ V and $f = 11.755$ GHz, corresponding to Fig. 2c in the main text, as shown in Supplementary Figure 5a. The coherence time T_2 was assumed to be 0.1 ns, and the peak conductance was set to be the same as the measurement. The abscissa (horizontal axis) was converted between P and V_{RF} using the relation:

$$V_{\mathrm{RF}} = \sqrt{\frac{50 * 10^{\frac{P}{10}}}{1000}}, \tag{S13}$$

where P is in dBm and V_{RF} in volts, and 50 Ω is the impedance. As plotted in Supplementary Figure 5b, the attenuation at this frequency can be achieved by a comparison between the calculated curve (green) and the measured curve (black). The two arrows mark the positions of the first peaks, and the attenuation was –61.6 + 16.1 = – 45.5 (dB). Note that the coaxial line passes through four attenuators (1 dB each), from the room temperature generator down to the mixing chamber. The 1 dB attenuator on each plate of the dilution refrigerator is used as a thermal sink, so that the coaxial lines can be cooled down well.

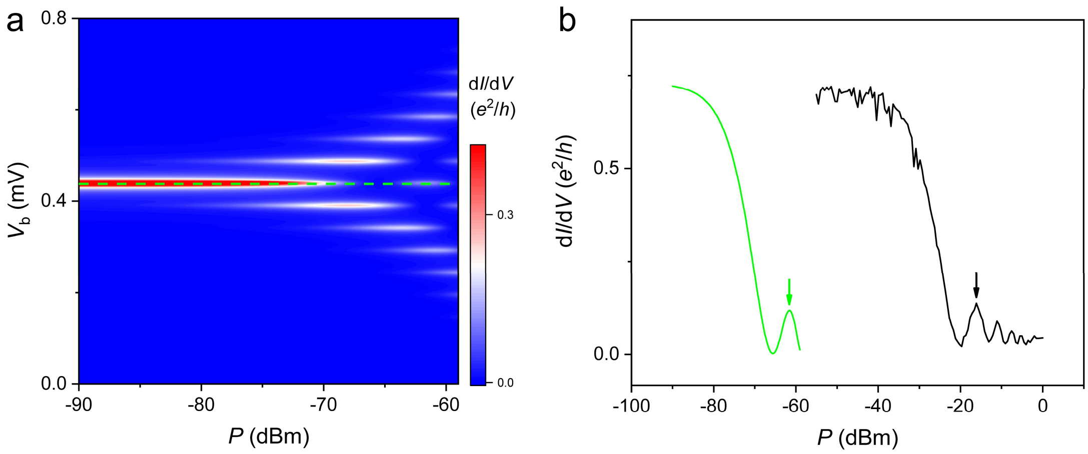

Supplementary Figure 5. Determination of the attenuation. a, Calculated interference fringes corresponding to Fig. 2c in the main text, without an attenuation of the microwave. **b**, Comparison between the experimental data (black curve) taken from Fig. 2c in the main text and the calculated (green) curve taken from **a**, as indicated by the green dashed line. An attenuation of –45.5 dB can be extracted by the power difference between the first peaks, as marked by the green and black arrows.

Step 2: select the proper data set and convert to the four quadrants.

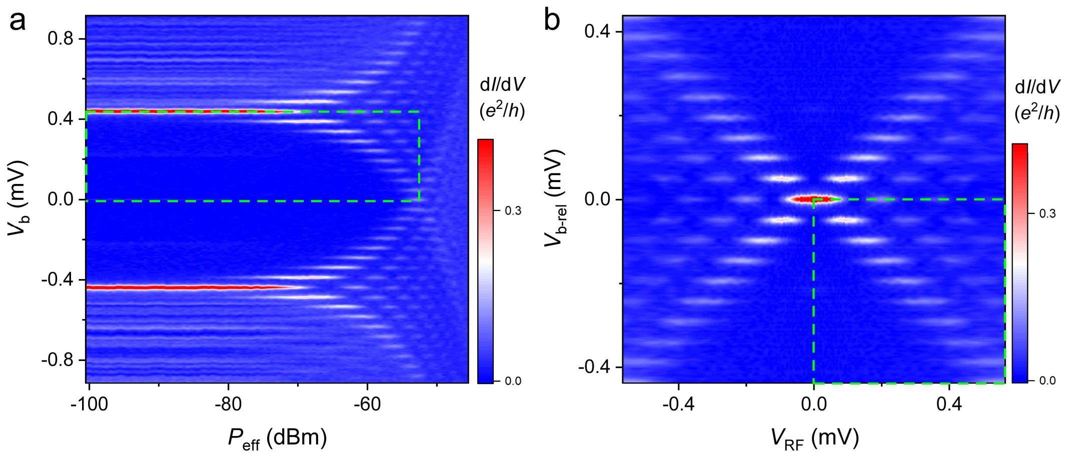

Supplementary Figure 6. Selecting the proper data set and converting to the four quadrants. a, The same data as in Fig. 2c in the main text, but with the effective microwave power $P_{\mathrm{eff}} = P - 45.5$ (dBm). The green dashed rectangle displays the data set chosen to perform the 2DFT. The coordinates of this data set were converted to the microwave amplitude V_{RF} and relative bias voltage $V_{\mathrm{b\text{-}rel}}$ by setting the $n = 0$ interference fringes to $V_{\mathrm{b\text{-}rel}} = 0$ mV, as indicated in **b** by the green dashed rectangle. The data set was further symmetrized to the four quadrants to carry out the 2DFT.

As shown by the green dashed rectangle in Supplementary Figure 6a, a clear part of the interference fringes was selected to carry out the 2DFT. The coordinates were converted and further symmetrized to the four quadrants, as displayed in Supplementary Figure 6b.

Step 3: perform the 2DFT.

To perform the 2DFT, according to the method explained in Supplementary Note 3, the coordinates of Supplementary Figure 6b were further scaled by $me\,V_{\mathrm{b-r}}$ and meV_{RF}, and the data were scaled to a maximum of 1. And then the 2DFT can be calculated as a function of k_ε and k_A, as shown in Fig. 2d in the main text. Note that an interpolation of the data was applied when a uniform coordinate spacing was needed.

The analysis of the other data sets of the interference fringes was performed following the same procedure as described above.

Supplementary Note 6. Effect of the magnetic field on the LZSM interference.

In this section, we present the effect of magnetic field on the LZSM interference and the coherence time. Supplementary Figure 7 shows a comparison of the interference fringes and the corresponding 2DFT patterns for the magnetic fields $B = 0$ T (Supplementary Figures 7a and 7b) and 0.2 T (Supplementary Figures 7c and 7d; along the nanowire). We can see that the interference fringes became blurred at $B = 0.2$ T, and the number of observable ovals decreased. Accordingly, the calculated coherence time T_2 dropped from ~ 0.057 ns to ~ 0.022 ns. We attribute such behavior to the softening of the induced superconducting gap in the InAsSb nanowire when a magnetic field is applied, which induces energy broadening and thus decoherence.

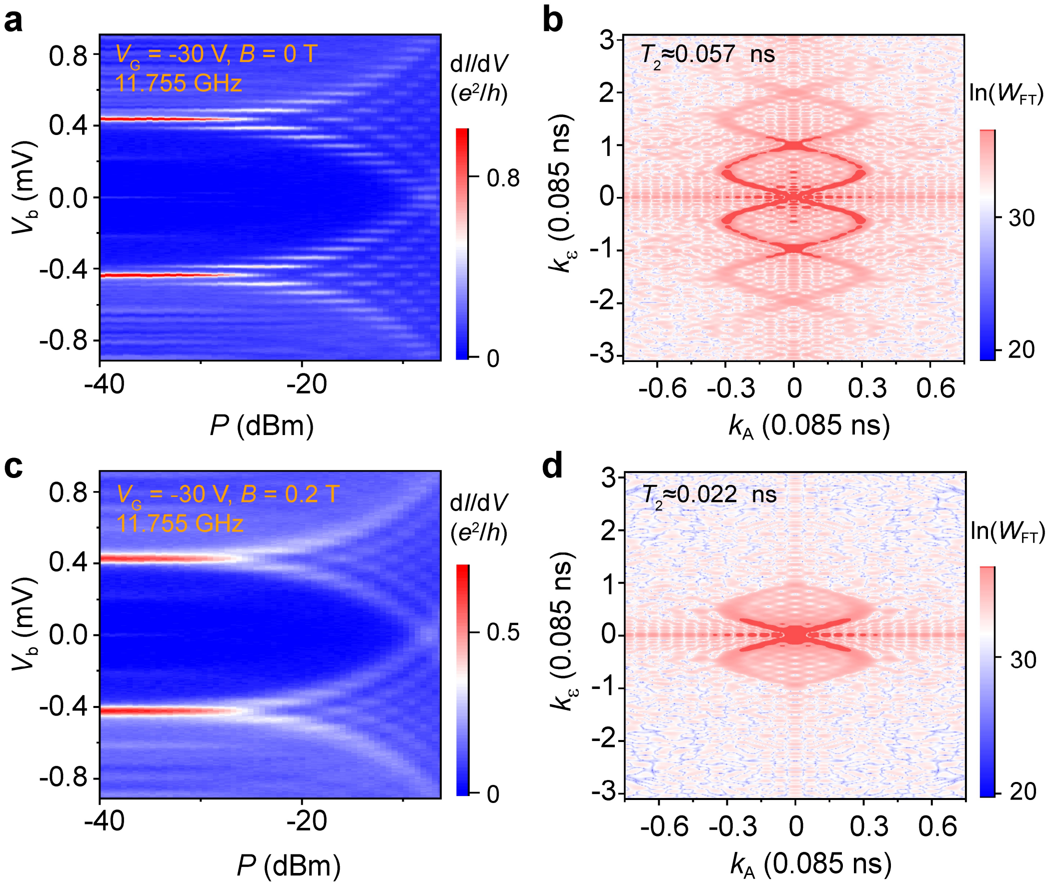

Supplementary Figure 7. Effect of the magnetic field on the LZSM interference. a, Interference fringes at $V_G = -30$ V, $B = 0$ T, and $f = 11.755$ GHz. **b**, 2DFT of **a**. **c**, The same as **a**, but at $B = 0.2$ T. **d**, 2DFT of **c**.

Supplementary Note 7. Correlated conductance quantization and critical supercurrent for the second Josephson junction (JJ2).

Supplementary Figure 8 shows the results for JJ2 (see Fig. 1 of the main text). The conductance dI/dV shown in the upper panel was measured in the normal state at a high-bias voltage: V_b=3 mV (black) and V_b=4.5 mV (red). The quantized conductance plateau at $2e^2/h$ demonstrates the single ballistic channel in the JJ. However, the plateau for $4e^2/h$ can be barely recognized, and the conductance evolves to the plateau of $6e^2/h$ when V_G increases. Such transition from a single channel to three channels could be attributed to the rotation symmetry of the nanowire which induces nearly degenerate 2nd and 3rd sub-bands, as has been observed in InSb nanowires[4].

The bottom panel shows the correlated critical supercurrent I_C, where a plateau of ~ 15 nA was achieved for a single ballistic channel, similar to JJ1 shown in the main text. The inset shows the dV/dI vs I curve at V_G = -10 V, and the arrow indicates the critical supercurrent.

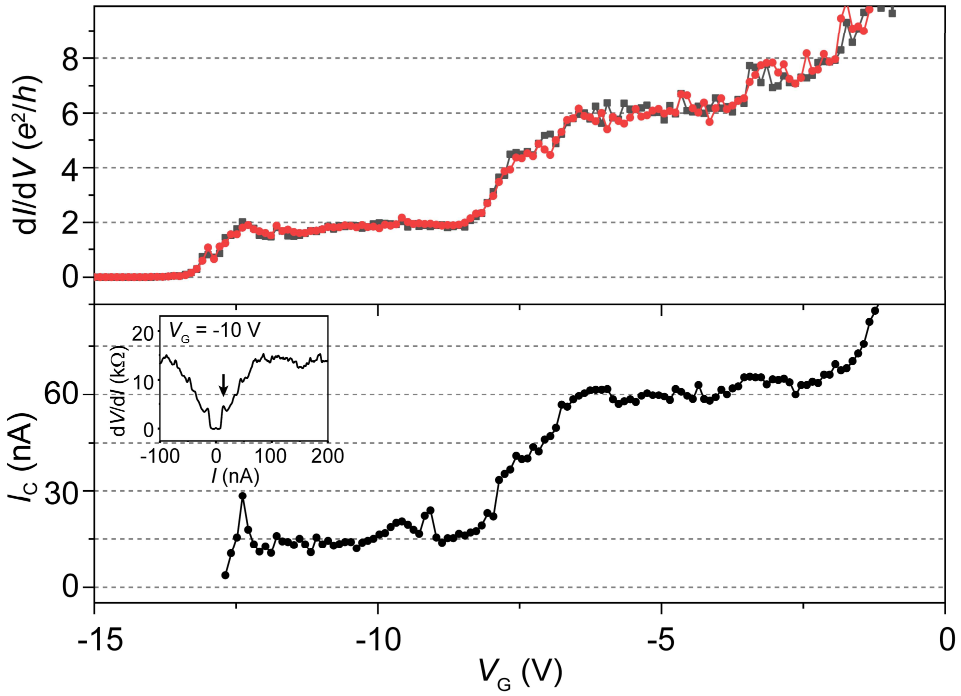

Supplementary Figure 8. Correlated conductance quantization and critical supercurrent for JJ2.

Supplementary Note 8. LZSM interference in another typical device.

LZSM interference can be regularly observed in naturally formed JJs. Supplementary Figure 9 shows the results of another typical device. An Al gap of ~ 50 nm was formed during the epitaxial growth of the Al shell due to the shadowing of the dense nanowires, as indicated by the red arrow in the scanning electron microscope image of the device shown in Supplementary Figure 9a. The side-gate voltage was set to 0 and a back-gate voltage V_G was applied to control the coupling strength. Supplementary Figure 9b displays the interference fringes of the Cooper pairs, 2-charges of the 1st-order multiple Andreev reflections, and single charges, similar to the one shown in the main text.

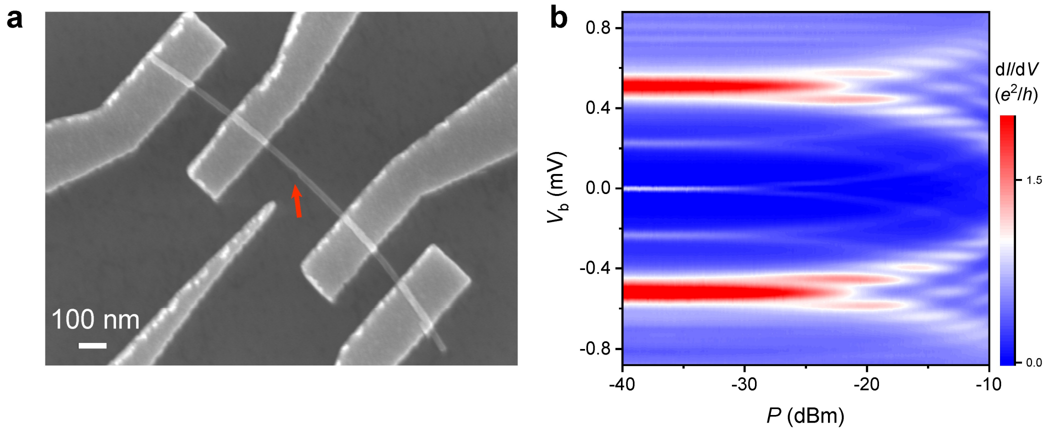

Supplementary Figure 9. LZSM interference in another device. a, Scanning electron microscope image of the device. The red arrow indicates the naturally formed Al gap which functions as the JJ. **b**, Typical interference fringes at a back-gate voltage $V_G = -3.6$ V (300 nm SiO_2), a zero side-gate voltage, and $f = 11.3$ GHz.

Supplementary References

1 Wen, L. *et al.* Large-Composition-Range Pure-Phase Homogeneous $InAs_{1-x}Sb_x$ Nanowires. *J. Phys. Chem. Lett.* **13**, 598-605, (2022).

2 Rudner, M. S. *et al.* Quantum Phase Tomography of a Strongly Driven Qubit. *Phys. Rev. Lett.* **101**, 190502, (2008).

3 González, S. A. *et al.* Photon-assisted resonant Andreev reflections: Yu-Shiba-Rusinov and Majorana states. *Phys. Rev. B* **102**, 045413, (2020).

4 Kammhuber, J. *et al.* Conductance Quantization at Zero Magnetic Field in InSb Nanowires. *Nano Lett.* **16**, 3482-3486, (2016).